Chapter 7
TEM Characterization of Lattice Defects Associated with Deformation and Fracture in α-Al_2O_3

Eita Tochigi, Bin Miao, Shun Kondo, Naoya Shibata, and Yuichi Ikuhara

7.1 Introduction

Alumina (α-Al_2O_3) is structural ceramics used for various applications such as refractory material, thermal coating, and film substrates. The mechanical behavior of alumina has been extensively investigated for decades. Discussion on microstructural plastic deformation mechanisms for single-crystalline alumina (sapphire) was started by Kronberg in 1957 (Kronberg 1957), who proposed dislocation behavior

E. Tochigi (✉) · B. Miao · S. Kondo · N. Shibata · Y. Ikuhara
Institute of Engineering Innovation, The University of Tokyo, 2-11-16 Yayoi, Bunkyo-ku, Tokyo 113-8656, Japan
e-mail: tochigi@sigma.t.u-tokyo.ac.jp

B. Miao
e-mail: miao@sigma.t.u-tokyo.ac.jp

S. Kondo
e-mail: kondou@sigma.t.u-tokyo.ac.jp

N. Shibata
e-mail: shibata@sigma.t.u-tokyo.ac.jp

Y. Ikuhara
e-mail: ikuhara@sigma.t.u-tokyo.ac.jp

E. Tochigi
PRESTO, Japan Science and Technology Agency, 4-1-8, Honcho, Kawaguchi, Saitama 332-0012, Japan

N. Shibata · Y. Ikuhara
Nanostructures Research Laboratory, Japan Fine Ceramics Center, 2-4-1, Mutsuno, Atsuta-ku, Nagoya 456-8587, Aichi, Japan

S. Kondo · Y. Ikuhara
Center for Elements Strategy Initiative for Structural Materials (ESISM), Kyoto University, Yoshidahonmachi, Sakyo-ku, Kyoto 606-8501, Japan

I. Tanaka et al. (eds.), *The Plaston Concept*,
https://doi.org/10.1007/978-981-16-7715-1_7

for the basal slip and basal twinning based on crystallographic considerations. Experimental characterizations of dislocations in deformed alumina crystals were actively performed by transmission electron microscopy (TEM) from the 1970s to 1990s (Pletka et al. 1974; Bilde-Sørensen et al. 1976, 1996; Mitchell et al. 1976; Firestone and Heuer 1976; Lagerlöf et al. 1984, 1994), and their structural details, such as Burgers vectors and dissociation reactions, have been revealed. These studies deepened my understanding of the plastic deformation processes of sapphire based on dislocation behavior. Since plastic deformation essentially corresponds to atomic rearrangement due to applied load, the atomistic behavior during plastic deformation has often been discussed, even by Kronberg. However, experimental evidence on atomic structures had not been obtained for years because of the lack of imaging techniques. With the development of TEM techniques, atomic-scale observations of dislocations in alumina were eventually realized since the 2000s, and their core atomic structures have been characterized so far (Nakamura et al. 2002, 2006; Ikuhara et al. 2003; Shibata et al. 2007; Heuer et al. 2010; Tochigi et al. 2010, 2011, 2012, 2015, 2016, 2017, 2018; Miao et al. 2019). Note that some of these studies examined dislocations in low-angle grain boundaries. The dislocation character characterized by Burgers vector and line direction can be controlled through the grain boundary orientation, and a dislocation equivalent to one introduced by plastic deformation can be easily obtained.

In situ TEM indentation experiment is a powerful technique to investigate microstructural evolution upon loading. Modern indentation holders for TEM are driven by a piezo actuator, and the indenter tip can be controlled in the sub-nanometer step (ex. PI-95, Bruker Corp.). To apply a load at a specific local area in a sample, deformation or fracture phenomena can be induced in a controlled manner. In general, in situ TEM indentation is performed in a conventional TEM because of the limitation of equipment compatibility. The experimental information is limited to the nanometer scale. Thus, post-mortem characterization by atomic-resolution TEM is often carried out to obtain detailed information at the atomic level. For alumina, crack propagation (Sasaki et al. 2012; Kondo et al. 2019) and dislocation formation phenomena (Miao et al. 2019) have been investigated by in situ indentation and atomic structure analysis so far.

In this report, we review our recent progress on structural analysis of lattice defects in alumina by TEM observations. In Sect. 7.2, the structures of dislocations with the Burgers vector $\boldsymbol{b} = 1/3 <11\bar{2}0>$, $<1\bar{1}00>$, and $1/3 <\bar{1}101>$ formed in low-angle grain boundaries are discussed based on experimental observations. In Sect. 7.3, the formation of a $1/3 <11\bar{2}0>$ mixed basal dislocation and fracture of Zr-doped $\{1\bar{1}04\}/<11\bar{2}0> \sum 13$ grain boundary are demonstrated by in situ TEM indentation experiments. These phenomena are further investigated at the atomic level based on atomic-resolution scanning TEM (STEM) observations performed after the indentation experiments.

7.2 Atomic Structure Analysis of Dislocations in Low-angle Boundaries

The plastic deformation of alumina is mainly produced by dislocation slip at elevated temperatures. The slip systems of alumina are known to be $(0001)1/3<11\bar{2}0>$ basal slip (Kronberg 1957; Pletka et al. 1974; Mitchell et al. 1976; Lagerlöf et al. 1984, 1994; Bilde-Sørensen et al. 1996; Nakamura et al. 2002; Shibata et al. 2007; Heuer et al. 2010; Miao et al. 2019), $\{11\bar{2}0\}<1\bar{1}00>$ prism-plane slip (Bilde-Sørensen et al. 1976; Lagerlöf et al. 1984), and $\{1\bar{1}02\}1/3<\bar{1}101>$ ($\{10\bar{1}1\}$ and $\{2\bar{1}\bar{1}3\}$ planes are also possible to be slip planes) pyramidal slip (Firestone and Heuer 1976). Thus, the $1/3<11\bar{2}0>$, $<1\bar{1}00>$, and $1/3<\bar{1}101>$ dislocations play an important role in the plastic deformation of alumina. Conventional TEM studies revealed that these dislocations are basically dissociated into some partial dislocations with stacking faults in between (Bilde-Sørensen et al. 1976; Mitchell et al. 1976; Lagerlöf et al. 1984, 1994). So far, their detailed atomic structures had not been well characterized.

Atomic-resolution TEM is a powerful technique to directly observe the atomic structure of a dislocation. Since this method provides a projected image of three-dimensional structures, the observed dislocation must be straight at end-on orientation. However, such dislocations are rarely found in a deformed crystal. Instead, low-angle grain boundaries can be used. They are divided into tilt and twist boundaries, which consist of an edge dislocation array and a screw dislocation network, respectively. The Burgers vector and line direction of the dislocations depend on the grain boundary orientation. Basically, an edge dislocation in a low-angle tilt grain boundary has the Burgers vector corresponding to the translation vector perpendicular to the boundary plane and line direction parallel to the rotation axis. A screw dislocation in a low-angle twist grain boundary has the Burgers vector and line direction corresponding to the smallest translation vector on the boundary plane. Based on these relationships, dislocation structures can be controlled through grain boundary orientation.

To obtain $1/3<11\bar{2}0>$, $<1\bar{1}00>$, and $1/3<\bar{1}101>$ dislocations, alumina bicrystals with the $\{11\bar{2}0\}/<1\bar{1}00>$, $(0001)/[0001]$, $(1\bar{1}00)/<11\bar{2}0>$, and $(0001)/<1\bar{1}00>$, low-angle grain boundary were fabricated by joining two pieces of single crystals at 1500 °C for 10 h in air. Thin foil samples with a grain boundary for TEM observations were prepared from the bicrystals by cutting, mechanical grinding, and Ar ion milling. The samples were observed by using conventional TEM (JEM-2010HC, 200 kV, JEOL), high-resolution TEM (HRTEM: JEM-4010, 400 kV, JEOL), and scanning TEM (STEM: ARM-200F, 200 kV, JEOL).

7.2.1 $1/3<11\bar{2}0>$ *Basal Edge Dislocation*

$1/3<11\bar{2}0>$ vector is the translation vector perpendicular to the $\{11\bar{2}0\}$ plane. It is considered that the $\{11\bar{2}0\}$ low-angle tilt grain boundary consists of $1/3<11\bar{2}0>$

edge dislocations. Figure 7.1 shows a bright-field TEM image of the $\{11\bar{2}0\}<1\bar{1}00>$ 2° low-angle tilt grain boundary. Dark contrast pairs periodically array in line with a separation distance of ~13 nm, suggesting that the $1/3 <11\bar{2}0>$ dislocation dissociates into two partial dislocations with a stacking fault in between. The tilt angle of the grain boundary 2θ and the dislocation configuration are related to Frank's formula, $2\theta = b/d$ (Frank 1951), where b is the magnitude of the Burgers vector of the perfect dislocation (0.476 nm) and d is the distance between the perfect dislocations. The tilt angle is estimated to be 2.1°, which agrees with the designed value. Previous TEM studies and crystallographic considerations revealed that the dissociation reaction of $1/3 <11\bar{2}0>$ dislocation follows the equation below (Mitchell et al. 1976; Lagerlöf et al. 1984, 1994; Ikuhara et al. 2003; Nakamura et al. 2006; Tochigi et al. 2008):

$$1/3 < 11\bar{2}0 > \rightarrow 1/3 < 10\bar{1}0 > +1/3 < 01\bar{1}0 > . \tag{7.1}$$

Figure 7.2 shows an HRTEM image of the $1/3 <11\bar{2}0>$ dislocation viewed along $<1\bar{1}00>$ direction. The two extra-half planes are located along [0001] direction with a separation distance of about 3 nm. This indicates that the dislocation consists of two partial dislocations with a stacking fault on $\{11\bar{2}0\}$ plane, although the stacking

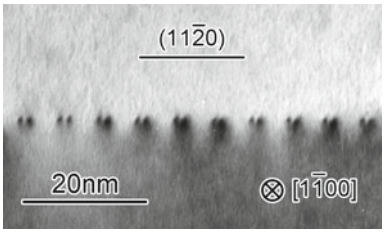

Fig. 7.1 TEM image of the $\{11\bar{2}0\}/<1\bar{1}00>$ 2° tilt grain boundary of alumina. Dislocation pairs periodically array along the grain boundary (Nakamura et al. 2006; Tochigi et al. 2008)

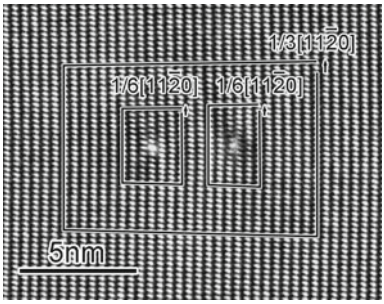

Fig. 7.2 HRTEM image of a dislocation pair viewed along $[1\bar{1}00]$ direction. The perfect dislocation dissociates into two partial dislocations with a stacking fault on $(11\bar{2}0)$ plane. The Burgers circuit indicates that the perfect dislocation has an edge component of $1/3[11\bar{2}0]$ and the partial dislocations have $1/6[11\bar{2}0]$ (Nakamura et al. 2006)

fault appears like the bulk in the present [$1\bar{1}00$] projection. Since the two partial dislocations are on different slip planes, this dissociation is found to occur by climb mechanism with atomic diffusion. Theoretical studies suggested that the formation energy of stacking faults (stacking fault energy) on the (0001) plane is at least one order higher than that on the {$11\bar{2}0$} plane (Y. 2008; Kenway 1993; Marinopoulos and Elsässer 2001). This would be the reason why the $1/3 <11\bar{2}0>$ edge dislocation does not dissociate on the (0001) plane by glide mechanism. The Burgers circuit shows the edge component of the partial dislocations is $1/6 <11\bar{2}0>$. This is consistent with the partial dislocations that have the Burgers vector of $1/3 <10\bar{1}0>$ and $1/3 <01\bar{1}0>$, the edge components of which are $1/6 <11\bar{2}0>$. The formation energy of the stacking fault (stacking fault energy) formed between two partial dislocations can be estimated from the separation distance based on the linear elastic theory. For a low-angle grain boundary, contributions from all the dislocations depending on their configurations need to be taken into account. In the present case, the stacking fault energy (γ) is calculated by the following equation (Ikuhara et al. 2003; Jhon et al. 2005):

$$\gamma = \frac{\mu b_p^2 (2+\nu)}{8\pi(1+\nu)} \cdot \frac{1}{d} \sum_{n=0}^{\infty} \left(\frac{1}{n+\alpha} - \frac{1}{n+1-\alpha} \right), \tag{7.2}$$

where μ is the shear modulus (~150 GPa (Nakamura et al. 2009)), b_p is the magnitude of the Burgers vector of the partial dislocations (0.275 nm), ν is Poisson's ratio (~0.24 (Chung and Simmons 1968)), and α is d_1/d (d_1: the spacing between the partial dislocations). Substituting the averaged values of $d = 13.2$ nm and $d_1 = 4.6$ nm into Eq. 7.2, the formation energy was estimated to be 0.32 Jm^{-2}, which agrees with the values estimated by HRTEM observations of a basal dislocation in a deformed crystal (0.28 Jm^{-2} (Nakamura et al. 2002)) and by first-principles calculations (0.35 Jm^{-2} (Marinopoulos and Elsässer 2001)). It can be said that analysis of low-angle boundaries is useful to obtain structural information of dislocation.

7.2.2 $1/3 <11\bar{2}0>$ *Basal Screw Dislocation*

Three equivalent translation vectors of $1/3 <11\bar{2}0>$ exist on the (0001) basal plane, and thus a (0001) low-angle twist grain boundary should consist of a network of $1/3 <11\bar{2}0>$ screw dislocations. Figure 7.3 shows a plan-view bright-field TEM image of a (0001)/[0001] low-angle twist grain boundary (Tochigi et al. 2012). A hexagonal dislocation network is observed. Since the dislocation line directions are parallel to either of [$11\bar{2}0$], [$1\bar{2}10$], and [$\bar{2}110$] directions, the dislocation network consists of the $1/3 <11\bar{2}0>$ screw dislocations. The periodicity of equivalent dislocations (d) is about 60 nm. The twist angle (φ) can be calculated to be 0.45°. To characterize the core atomic structure of the $1/3 <11\bar{2}0>$ screw dislocation, a $<11\bar{2}0>$ cross-sectional sample was prepared and observed by HRTEM. Figure 7.4 shows the core atomic structure of the $1/3 <11\bar{2}0>$ screw dislocation. A little contrast

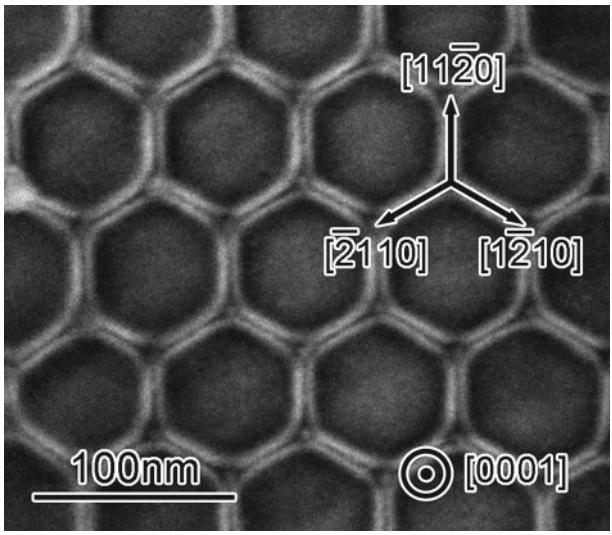

Fig. 7.3 Plan-view TEM image of the (0001)/[0001] twist grain boundary of alumina. A hexagonal dislocation network is formed. The line direction of dislocations is either of [11$\bar{2}$0], [1$\bar{2}$10], and [$\bar{2}$110], indicating that they are 1/3 <11$\bar{2}$0> screw dislocations (Tochigi et al. 2012)

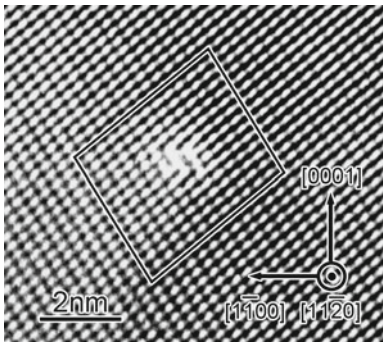

Fig. 7.4 HRTEM image of 1/3 <11$\bar{2}$0> screw dislocation viewed end on. The lattice disorder at the center corresponds to the dislocation core. The circuit without disconnection shows that it is the perfect screw dislocation (Tochigi et al. 2012)

disorder appears at the center without any lattice discontinuities as shown by the closed circuit, indicating the presence of the screw dislocation. This screw dislocation is in the perfect type in contrast to the basal edge dislocation consisting of the partial dislocation pair. If the screw dislocation dissociates by climb mechanisms following Eq. 7.1, the accumulation of extra atoms or vacancies between partial dislocations is structurally required. This process may need high energy and is difficult to occur. A more detailed discussion on the dissociation mechanisms of basal dislocations will be given in Sect. 7.3.1.

7.2.3 $<1\bar{1}00>$ Edge Dislocation

Figure 7.5 shows a bright-field TEM image of a $\{1\bar{1}00\}/<11\bar{2}0>$ low-angle 2° tilt grain boundary (Tochigi et al. 2010, 2016). Dark contrast triplets periodically array in line. Since the translation vector normal to the $\{1\bar{1}00\}$ plane is $<1\bar{1}00>$, the dark contrast triplet is originated from the $1/3<1\bar{1}00>$ partial dislocation triplets formed by the following dissociation reaction:

$$< 1\bar{1}00 > \rightarrow 1/3 < 1\bar{1}00 > +1/3 < 1\bar{1}00 > +1/3 < 1\bar{1}00 > . \tag{7.3}$$

Figure 7.6 shows an HRTEM image of the $1/3<1\bar{1}00>$ partial dislocation triplet. The partial dislocations are located along the [0001] direction with separation distances of approximately 10.1 and 10.9 nm from the left-hand side. Two stacking faults are formed on the $\{1\bar{1}00\}$ plane, and they are structurally inequivalent (Lagerlöf et al. 1984). As a result of detailed analysis, it was found that the left stacking fault has the stacking sequence of …ABCCABC… referred to as I_2 type, and the right one has …ABCBCABC… referred to as V type (Tochigi et al. 2010). In the present case, their stacking fault energies can be calculated by the following equations:

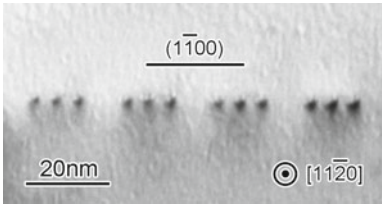

Fig. 7.5 TEM image of the $\{1\bar{1}00\}/<11\bar{2}0>$ 2° tilt grain boundary of alumina. The grain boundary consists of dislocation triplets (Tochigi et al. 2010)

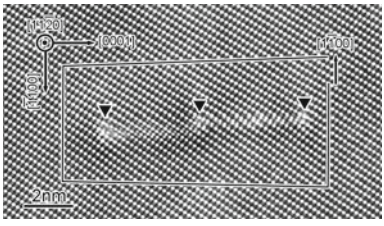

Fig. 7.6 HRTEM image of a dislocation triplet view along $[11\bar{2}0]$. The circuit shows that the perfect dislocation has the Burgers vector of $[1\bar{1}00]$. The stacking faults are formed on $\{1\bar{1}00\}$ plane. A detailed analysis found that the left stacking fault has the staking sequence of …ABCCABC… (I_2 type) and the right one has …ABCBCABC… (V type) (Tochigi et al. 2010)

$$\gamma_{I2} = \frac{\mu b_p^2}{2\pi(1-\nu)} \cdot \frac{1}{d} \sum_{n=0}^{\infty} \left(\frac{1}{n+\alpha_1} + \frac{1}{n+\alpha_1+\alpha_2} - \frac{1}{n+1-\alpha_1} - \frac{1}{n+1-\alpha_1-\alpha_2} \right), \quad (7.4)$$

$$\gamma_V = \frac{\mu b_p^2}{2\pi(1-\nu)} \cdot \frac{1}{d} \sum_{n=0}^{\infty} \left(\frac{1}{n+\alpha_2} + \frac{1}{n+\alpha_1+\alpha_2} - \frac{1}{n+1-\alpha_2} - \frac{1}{n+1-\alpha_1-\alpha_2} \right), \quad (7.5)$$

where α_1 is d_1/d (d_1: the width of stacking fault I_2) and α_2 is d_2/d (d_2: the width of stacking fault V). Substituting the experimental averaged values of $d = 22$ nm, $d_1 = 4.9$ nm, and $d_2 = 5.7$ nm, into Eqs. (7.4) and (7.5), the stacking fault energies $\gamma_{I2} = 0.44\ \mathrm{Jm}^{-2}$ and $\gamma_V = 0.35\ \mathrm{Jm}^{-2}$, which agree with the values estimated by theoretical studies using first-principles calculations, 0.46 and 0.41 Jm^{-2}. Note that the $<1\bar{1}00>$ edge dislocation associated with $\{11\bar{2}0\}<1\bar{1}00>$ slip has the line direction along the [0001] direction and is not structurally equivalent to the dislocation characterized here. The slip dislocation is also known to dissociate into three partial dislocations with $\{1\bar{1}00\}$ stacking faults following Eq. (7.3) (Bilde-Sørensen et al. 1976; Lagerlöf et al. 1984). These stacking faults should be I_2 and V types, although no direct evidence has ever been obtained. This is because the other possible $\{1\bar{1}00\}$ stacking fault …ABCBABC… referred to as I_1 type is calculated to have the formation energy of 0.62–0.63 Jm^{-2}, which is about 1.4–1.8 times higher than that of I_2 and V types (Tochigi et al. 2010; Marinopoulos and Elsässer 2001).

7.2.4 1/3 <$\bar{1}$101> *Mixed Dislocation*

Figure 7.7 shows a TEM image of the $(0001)/<1\bar{1}00>$ 2° tilt grain boundary (Tochigi et al. 2015). Bright discrete contrasts are observed along the grain boundary, suggesting that dislocations array periodically. An HRTEM image of the grain boundary is shown in Fig. 7.8. Dislocation contrasts are seen, and each dislocation is elongated on the (0001) plane with a separation distance of about 4 nm, indicating that the dislocation dissociates into two partial dislocations with a (0001) stacking fault. The Burgers circuits drawn around the dislocations indicate that the dislocations have the edge component of either 1/3[0001], 1/6[$\bar{1}\bar{1}$22], or 1/6[11$\bar{2}$2]. Since these components do not coincide with a translation vector, the dislocations should be the mixed type having a screw component along the [$1\bar{1}$00] direction. The

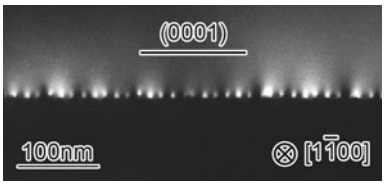

Fig. 7.7 TEM image of the $(0001)/<1\bar{1}00>$ 2° tilt grain boundary of alumina. Bright contrasts are periodically seen along the boundary (Tochigi et al. 2015)

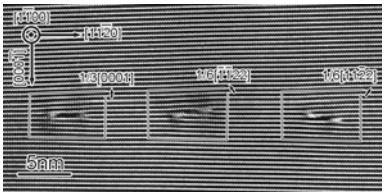

Fig. 7.8 HRTEM image of the grain boundary viewed edge on. Three dislocations having an edge component of 1/3[0001], 1/6[$\bar{1}\bar{1}$22], and 1/6[11$\bar{2}$2] are observed. Each dislocation dissociates into two partial dislocations with stacking fault on (0001) plane (Tochigi et al. 2015)

screw components can be identified based on crystallography. For the case of the edge component of 1/6[$\bar{1}\bar{1}$22], considering the formula 1/6[$\bar{1}\bar{1}$22] + n[1$\bar{1}$00], it equals to the smallest translation vector of 1/3[0$\bar{1}$11] for $n = 1/6$. Thus, the screw component and the total Burgers vector are identified to be 1/6[1$\bar{1}$00] and 1/3[0$\bar{1}$11], respectively. Similarly, for the cases of 1/6[11$\bar{2}$2], and 1/3[0001], the total Burgers vectors were found to be 1/3[10$\bar{1}$1] and 1/3[$\bar{1}$101], respectively. The sum of 1/3[0$\bar{1}$11], 1/3[10$\bar{1}$1], and 1/3[$\bar{1}$101] is [0001], which is the translation vector perpendicular to the (0001) grain boundary plane. In the present boundary, it was found that three equivalent mixed dislocations accommodate the grain boundary misorientation.

Figure 7.9 shows an annular bright-field (ABF) STEM image of the 1/3[0$\bar{1}$11] dislocation. In this image, dark contrasts correspond to atomic columns as indicated by the atomic model overlaid. The edge components of the partial dislocations are found to be 1/18[$\bar{1}\bar{1}$23] and 1/18[$\bar{2}\bar{2}$43], and the stacking fault formed on the (0001) plane has the stacking sequence of …2B 1 2C 3 1A 2 1B 3…. The Burgers vector of the partial dislocations can be estimated through the fault vector of the stacking fault. A detailed analysis using first-principles calculations revealed the fault vector

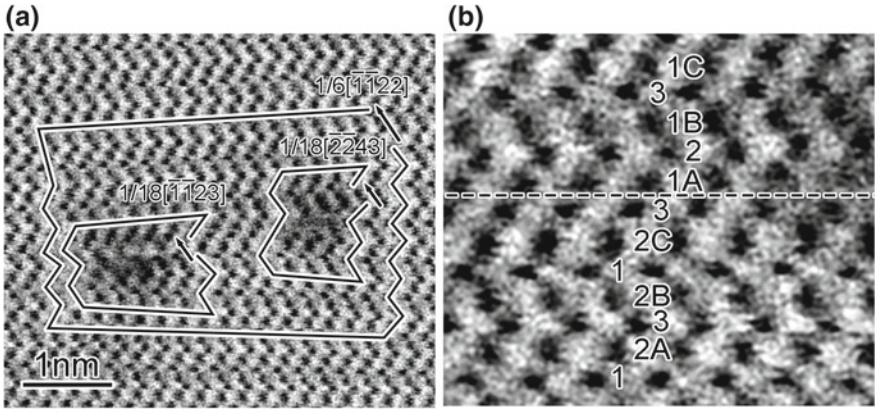

Fig. 7.9 **a** ABF-STEM image of the dislocation with the edge component of 1/6[$\bar{1}\bar{1}$22]. The edge component of two partial dislocations are 1/18[$\bar{2}\bar{4}$23] and 1/18[$\bar{2}\bar{2}$43]. **b** Enlarged image of (0001) stacking fault. Its stacking sequence is …2B 1 2C 3 1A 2 1B 3… (Tochigi et al. 2015)

of the stacking fault, and the Burgers vectors of the partial dislocations were found to be $1/18[2\bar{4}23]$ and $1/18[\bar{2}\bar{2}43]$ (Tochigi et al. 2015). The dissociation reaction of $1/3 <0\bar{1}11>$ dislocation is described by the following equation:

$$1/3 < 0\bar{1}11 > \rightarrow 1/18 < 2\bar{4}23 > +1/18 < \bar{2}\bar{2}43 > . \tag{7.6}$$

It was confirmed that the dissociation of the other two cases is also given by Eq. (7.6) (Tochigi et al. 2015). The stacking fault energy was estimated to be experimentally 0.58 Jm^{-2} and theoretically 0.72 Jm^{-2}, and they agree with each other. The $1/3 <0\bar{1}11>$ dislocation was found to dissociate on the (0001) plane, not corresponding to the slip plane. Therefore, the $1/3 <0\bar{1}11>$ dislocations may become immobile by the dissociation reaction.

7.3 Analysis of Dislocation Formation and Grain Boundary Fracture by in Situ TEM Nanoindentation and Atomic-Resolution STEM

To directly observe the dynamic behavior of lattice defects upon loading, in situ TEM mechanical experiment is an efficient method. In this section, the formation process of a basal dislocation (Miao et al. 2019) and the propagation process of a crack along a large angle grain boundary of alumina (Kondo et al. 2019) are demonstrated by an in situ TEM nanoindentation experiment. Furthermore, the nucleated defects were statistically characterized by STEM after the nanoindentation experiment to develop an atomistic understanding of their formation processes.

7.3.1 Introduction of a Basal Mixed Dislocation and Its Core Structure

The $(0001)1/3 <1\bar{2}10>$ basal slip becomes to be the easiest slip system at elevated temperature >~1000 °C (Lagerlöf et al. 1994). In addition, the core structures of the $1/3 <1\bar{2}10>$ basal dislocation in different orientation have been investigated for approximately 20 years. So far, atomic-resolution TEM/STEM studies characterized the dislocation core structures in edge (Nakamura et al. 2002, 2006; Shibata et al. 2007; Heuer et al. 2010), 30° (Heuer et al. 2010), and screw (Tochigi et al. 2012) types. However, the core structure of 60° mixed dislocation has not been observed yet. Here, we demonstrate the formation process and core structure of the 60° mixed dislocation (Miao et al. 2019).

An alumina single crystal plate was mounted on a half-moon-shaped mesh and thinned by mechanical grinding. The sample was further milled by Ar ion milling until its free edge obtains electron transparency. The face of the sample was parallel

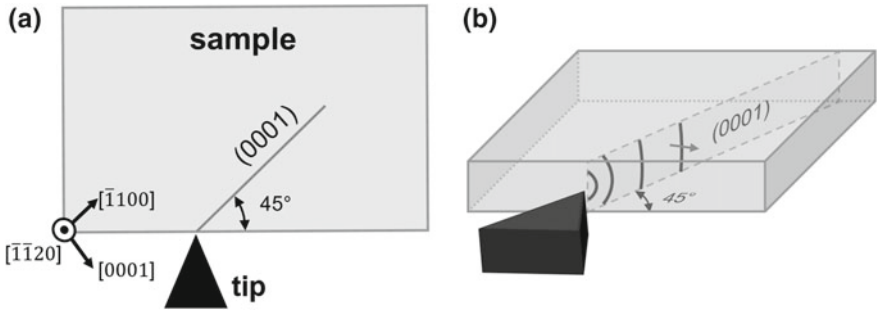

Fig. 7.10 Schematic illustrations showing the crystallographic orientation of the sample and the indentation direction. **a** The indentation direction was set at an angle of 45° from (0001) plane. **b** 3D illustration. The red arrow indicates the Burgers vector of dislocation expected to be induced by indentation, which is $1/3[1\bar{2}10]$ (Miao et al. 2019)

to the $(11\bar{2}0)$ plane and the free edge was set at an angle of 45° from the (0001) plane, as illustrated in Fig. 7.10. The indentation direction was set perpendicular to the free edge. Assuming a unidirectional force, the $(0001)1/<1\bar{2}10>$ basal slip has the largest Schmid factor of 0.5. In situ TEM nanoindentation experiment was performed using a nanoindentation TEM sample holder (Nanofactory Instruments AB, Sweden) in a conventional TEM (JEM-2100HC, 200 kV, JEOL). After the nanoindentation experiment, the sample was further thinned by Ar ion milling at liquid nitrogen temperature to get the deformed area thin. The core atomic structure of introduced dislocations was observed by atomic-resolution STEM (ARM-200F, 200 kV, JEOL).

Figure 7.11 shows TEM images taken before and after indentation. The alumina sample is seen at the upper part of the image and the indenter tip is below. Before indentation, no obvious defects are included in the sample (Fig. 7.11a). After indentation, bend contours are seen over the sample and the sample edge is chipped, where a strong indentation force was expected to be applied (Fig. 7.11b). The straight dark contrast is generated from the chipped area and is parallel to (0001), suggesting that basal slip was activated and some basal dislocations were formed there. To characterize the basal dislocations in detail, the sample was mounted on a double tilt sample holder and the indented area was observed with tilt-controlled conditions. Figure 7.11c shows a bright-field TEM image taken along the $[11\bar{2}0]$ zone axis. Two dotted contrast features are seen at the end of the straight contrast. These features were observed along the $[22\bar{4}1]$ direction by tilting the sample by 24.5 degrees around the $[1\bar{1}00]$ axis (Fig. 7.11d). They appear as curved lines and are found to be basal dislocations.

Figure 7.12a shows an ABF-STEM image of one of the dislocations induced by the nanoindentation experiment. The dislocation was observed along the $[11\bar{2}0]$ direction and found to dissociate into two partial dislocations with a separation distance of approximately 2.9 nm. A stacking fault is formed on the $\{1\bar{1}00\}$ plane, and this dissociation also occurred by climb. The largest Burgers circuit shows that

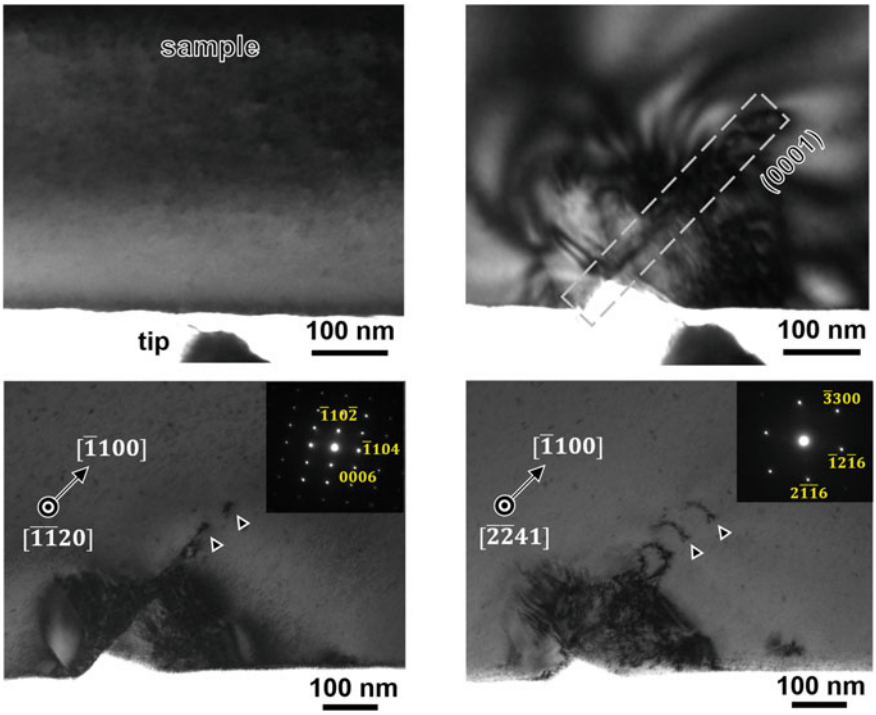

Fig. 7.11 TEM images of the sample before and after the indentation experiment. **a** Before indentation. The sample exhibits a uniform contrast and seems to have no obvious defects. **b** After indentation. The sample edge is chipped due to the insertion of the indenter tip. A straight contrast parallel to (0001) plane from the top of the chipped region, indicating that (0001) slip system was activated. **c** Bright-field image of the indented sample viewing along [11$\bar{2}$0] direction. Two dotted contrasts are seen along (0001) plane. **d** [$\bar{2}\bar{2}$41] view of the sample, where it was rotated by 24.5 degrees around [$\bar{1}$100] axis. The dotted contrasts in (**c**) become curved contrasts, indicating they correspond to basal dislocations (Miao et al. 2019)

the perfect dislocation has an edge component of 1/6[1$\bar{1}$00]. Since this component does not correspond to a translation vector, the perfect dislocation should have a screw component along the [11$\bar{2}$0] direction. From crystallographic considerations, the screw component can be determined in order to get the smallest translation vector, which is 1/6 <11$\bar{2}$0>. Therefore, the perfect dislocation is identified to be 1/3 <1$\bar{2}$10> 60° mixed dislocation. In Fig. 7.12a, the small Burgers circuits indicate that the edge components of the upper and lower partial dislocations are 1/3[1$\bar{1}$00] and 1/6[1$\bar{1}$00], respectively. Since the dissociation reaction follows Eq. (7.1), it is considered that the upper partial dislocation is 1/3[1$\bar{1}$00] edge dislocation and the lower dislocation is 1/3[01$\bar{1}$0] 30° mixed dislocation. The crystallographic orientation of this dissociated dislocation on the (0001) plane is illustrated in Fig. 7.12b. The vectors of 1/3[1$\bar{2}$10], 1/6[1$\bar{1}$00], and 1/6[01$\bar{1}$0] are drawn in the green, blue, and red arrows. The [11$\bar{2}$0] projection of these vectors coincides with the edge component

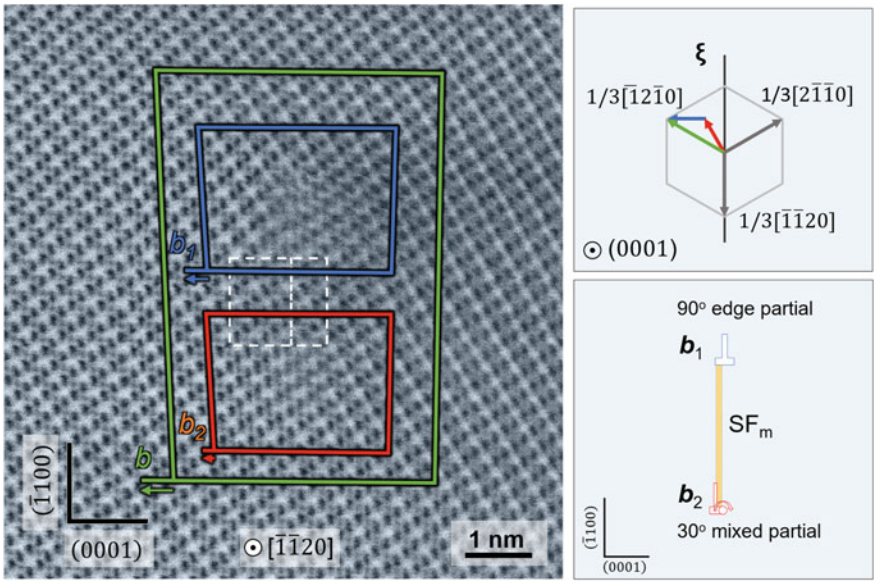

Fig. 7.12 **a** ABF-STEM image of a basal dislocation viewing along $[\bar{1}\bar{1}20]$ direction, which was introduced by the indentation experiment. The dislocation dissociates into two partial dislocations with $\{1\bar{1}00\}$ stacking fault by climb. $\boldsymbol{b}$, $\boldsymbol{b_1}$, and $\boldsymbol{b_2}$ correspond to the vector of 1/3 $[\bar{1}2\bar{1}0]$, 1/3 $[\bar{1}100]$, and $1/3[01\bar{1}0]$, and their edge components 1/2 $[\bar{1}100]$, 1/3 $[\bar{1}100]$, and 1/6 $[\bar{1}100]$ are seen in the image. **b** Schematic illustration showing (0001) projection of the Burgers vectors. Green, blue, and red arrows correspond to $\boldsymbol{b}$, $\boldsymbol{b_1}$, and $\boldsymbol{b_2}$, respectively. The viewing or dislocation line direction is represented by $\boldsymbol{\xi}$. **c** Schematic illustration showing the dissociated structure of the 1/3 $[\bar{1}2\bar{1}0]$ 60° mixed dislocation, which consists of 90° edge and 30° mixed partial dislocations (Miao et al. 2019)

of the dislocations shown in Fig. 7.12a. The dissociated structure observed along $[11\bar{2}0]$ is schematically illustrated in Fig. 7.12c.

Figure 7.13 shows magnified images of the bulk and the $\{1\bar{1}00\}$ stacking fault formed between the partial dislocations. The position of the stacking fault is indicated by the dashed line, and structural features are indicated by the circles. In comparison with the experimental image and the structure model, the stacking sequence is identified to be …ABCBCABC… referred to as V type as mentioned in Sect. 7.2.3 (Lagerlöf et al. 1984; Tochigi et al. 2010, 2016; Marinopoulos and Elsässer 2001). The stacking fault energy can be estimated by the following equation:

$$\gamma = \frac{\mu b_p^2 (2-\nu)}{8\pi d_1 (1-\nu)} \left(1 - \frac{2\nu - cos2\beta}{2-\nu}\right), \tag{7.7}$$

where β means the angle between the total Burgers vector and dislocation line direction. Substituting the separation distance $d_1 = 2.9$ nm and $\beta = 60°$, the stacking fault energy is 0.41 Jm^{-2}, which agrees well with the experimental and theoretical values of 0.35 Jm^{-2} and 0.41 Jm^{-2} estimated in Sect. 7.2.3.

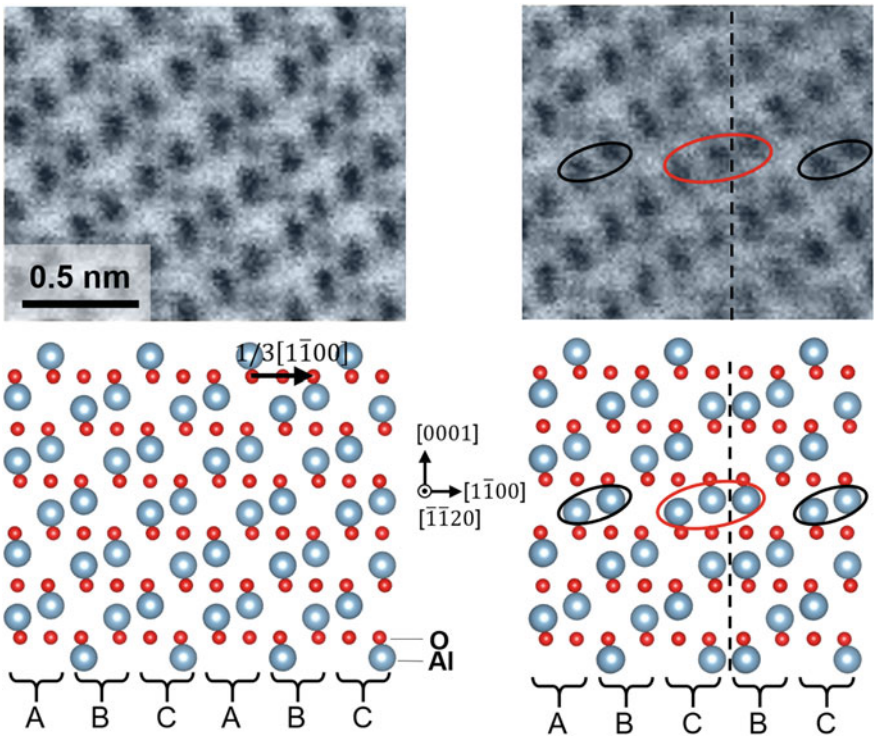

Fig. 7.13 Enlarged ABF-STEM image and atomic structure model of **a** bulk region and **b** {1$\bar{1}$00} stacking fault formed between the partial dislocations. The position of the stacking fault is indicated by dashed lines. The stacking sequence is …ABCBC… corresponding to V-type. The red ellipse shows structural features of the stacking fault (Miao et al. 2019)

The present experiment revealed the core structure of 60° mixed basal dislocation, and thus the core structures of the edge, 30°, 60°, and screw basal dislocations have been experimentally identified, which are summarized in Fig. 7.14. The edge, 60° mixed and 30° mixed basal dislocations dissociate into two partial dislocations following Eq. (7.1). The dissociation of the edge and 60° mixed dislocations occur by climb, while that of the 30° mix dislocation occurs by cross slip because one of the partial dislocations is screw type. Their stacking fault plane is perpendicular to the basal plane, which is the {11$\bar{2}$0} plane for the edge and 30° dislocations and the {1$\bar{1}$00} plane for the 60° mixed dislocation. These dissociation reactions occur by climb rather than glide. A possible reason is that the stacking faults formed on the (0001) plane are predicted to have one order higher energy than the $\{11\bar{2}0\}$ and {1$\bar{1}$00} stacking faults (Y. 2008; Kenway 1993; Marinopoulos and Elsässer 2001). The screw basal dislocation does not dissociate and has the perfect type of core structure. Considering geometric relationship and stability of stacking fault, the screw dislocation is possible to dissociate with the {1$\bar{1}$00} stacking fault in V type as illustrated in Fig. 7.13e. However, to form this dissociated structure, accumulation

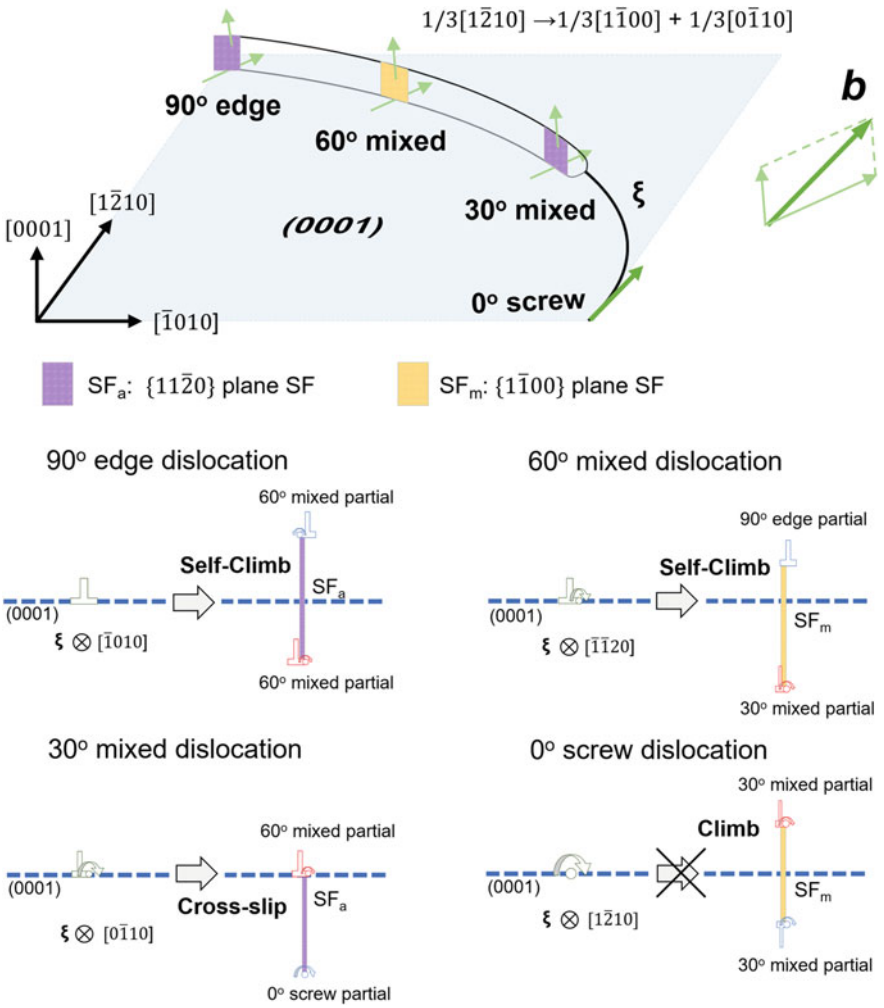

Fig. 7.14 Schematic illustrations showing dissociated structures of a basal dislocation in alumina. **a** A curved 1/3[1$\bar{2}$10] dislocation containing the 90°, 60°, 30°, 0° parts. The former three parts are dissociated into 1/3[1$\bar{1}$00] and 1/3[01$\bar{1}$0] partial dislocations. **b** 90° dislocation. Its dissociation occurred by climb with the{1$\bar{2}$10} stacking fault. The two partial dislocations have 60° orientation. **c** 60° dislocation. Its dissociation occurred by climb with the{1$\bar{1}$00} stacking fault. The two partial dislocations have 90° and 30° orientation. **d** 30° dislocation. Its dissociation occurred by cross-slip with the {1$\bar{2}$10} stacking fault. The two partial dislocations have 60° and 0° orientation. **e** 0° dislocation. From geometrical considerations, this dislocation can dissociate into 30° partial dislocations, but it does not occur experimentally (Miao et al. 2019)

of vacancies between the partial dislocations is necessary, which could be difficult to realize. This would be the reason why the screw dislocation does not dissociate.

7.3.2 Crack Propagation Along Zr-Doped ∑13 Grain Boundary

Polycrystalline materials are often fractured along grain boundaries. This suggests that grain boundaries can preferentially be a crack propagation path, and the atomic bonding of the grain boundaries is weaker than that of the bulk. However, little is known about the atomistic mechanisms of grain boundary fracture phenomena because of the lack of experimental examinations. In this section, we demonstrate the fracture experiment of a well-oriented grain boundary in TEM (Kondo et al. 2019). The Zr-doped $\{1\bar{1}04\}/<11\bar{2}0>$ ∑13 grain boundary of alumina was prepared by the bicrystal method. Crack propagation along the grain boundary was induced and directly observed by the in situ TEM nanoindentation technique. The fracture surfaces were further characterized by atomic-resolution STEM and first-principles calculations. The mechanisms for the grain boundary fracture will be discussed in terms of the atomic bonding of the grain boundary.

Two pieces of alumina single crystal were precisely cut so as to have the orientation relationship of $\{1\bar{1}04\}/<11\bar{2}0>$ ∑13. The bonding surface of one of them was coated by Zr with about 5 nm thickness using an Ar ion spattering machine. The two crystals were joined to be a bicrystal at 1500 °C for 30 h in air. A small plate including the grain boundary was cut from the bicrystal block and mounted on a half-moon-shaped mesh. The sample was thinned by mechanical grinding and Ar ion milling. Nanoindentation experiments were performed using a double-tilt nanoindentation TEM holder (Nanofactory) and a conventional TEM (JEM-2010HC, 200 kV, JEOL). The indenter tip was inserted along the grain boundary to preferentially induce grain boundary fracture. The indented sample was further observed by atomic-resolution STEM (ARM-200F, 200 kV, JEOL) to characterize the atomic structure of the fractured region. The fracture path was further investigated by first-principles calculations. Firstly, a supercell with the Zr-doped Σ13 grain boundary containing 196 atoms was constructed based on experimental observations. This model was optimized using the VAPS program (Gieske and Barsch 1968) under the generalized gradient approximations (Kresse and Furthmüller 1996). A $3 \times 2 \times 1$ k-point mesh and the energy cutoff of 500 eV were used. Secondly, atomic models of three kinds of fracture surfaces were constructed in order to remove half of the atoms from the optimized supercell. The total energies of these supercells were calculated without structural optimization to estimate the cleavage energies. Thirdly, the structural optimization was carried out for these supercells, and the optimized structures were compared with an experimental image.

Figure 7.15 shows sequential TEM images captured from a movie taken during the nanoindentation experiment. Figure 7.15a shows an image before indentation.

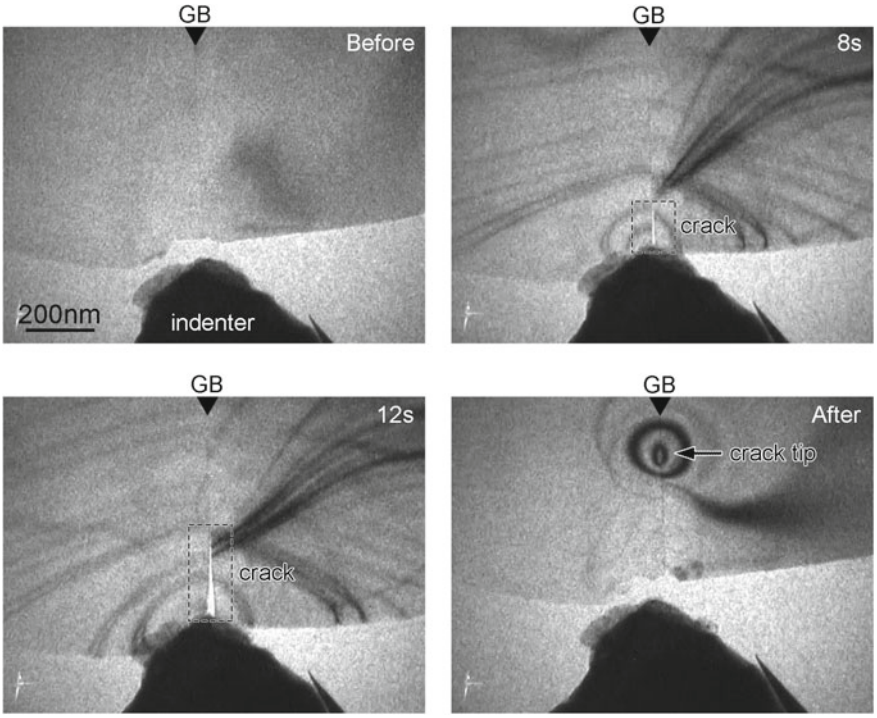

Fig. 7.15 Sequential images captured from a movie taken during in situ TEM nanoindentation experiment. **a** Before indentation. The grain boundary is located vertically in the middle of the sample. **b** After 8 s. The indentation started. A crack initiated along the grain boundary from the sample edge. **c** After 12 s. The crack propagated. **d** After the indenter retracted. Characteristic rounded contrasts are seen in the sample, corresponding to bend contours. The crack tip is expected to be located at their center (Kondo et al. 2019)

The sample and indenter tip are observed. The grain boundary is located vertically in the middle. In 8 s (Fig. 7.15b), a crack is found to nucleate from the top of the indenter tip as indicated by the dashed box in the figure. In 12 s, the crack propagates along the grain boundary (Fig. 7.15c). Figure 7.15d shows a situation after the indentation experiment. The rounded contrasts are seen as pointed by the arrow. They should be bend contours, and thus the crack tip is expected to have propagated around the center of the rounded contrasts.

The indented sample was directly transferred to atomic-resolution STEM. Figure 7.16 shows a high-angle annular dark-field (HAADF) STEM image of the vicinity of crack tip (Fig. 7.16a) and one of the fracture surfaces (Fig. 7.16b). In the HAADF images, strong and weak spots correspond to Zr and Al columns, respectively. In the upper part of Fig. 7.16a corresponding to the unfractured area, three layers of Zr are formed along the grain boundary, namely that Zr forms the segregation structure of three atomic layers in the $\{1\bar{1}04\}/<11\bar{2}0>$ $\sum 13$ grain boundary of alumina. In the lower part, the Zr segregation layers appear a little fuzzy and consist

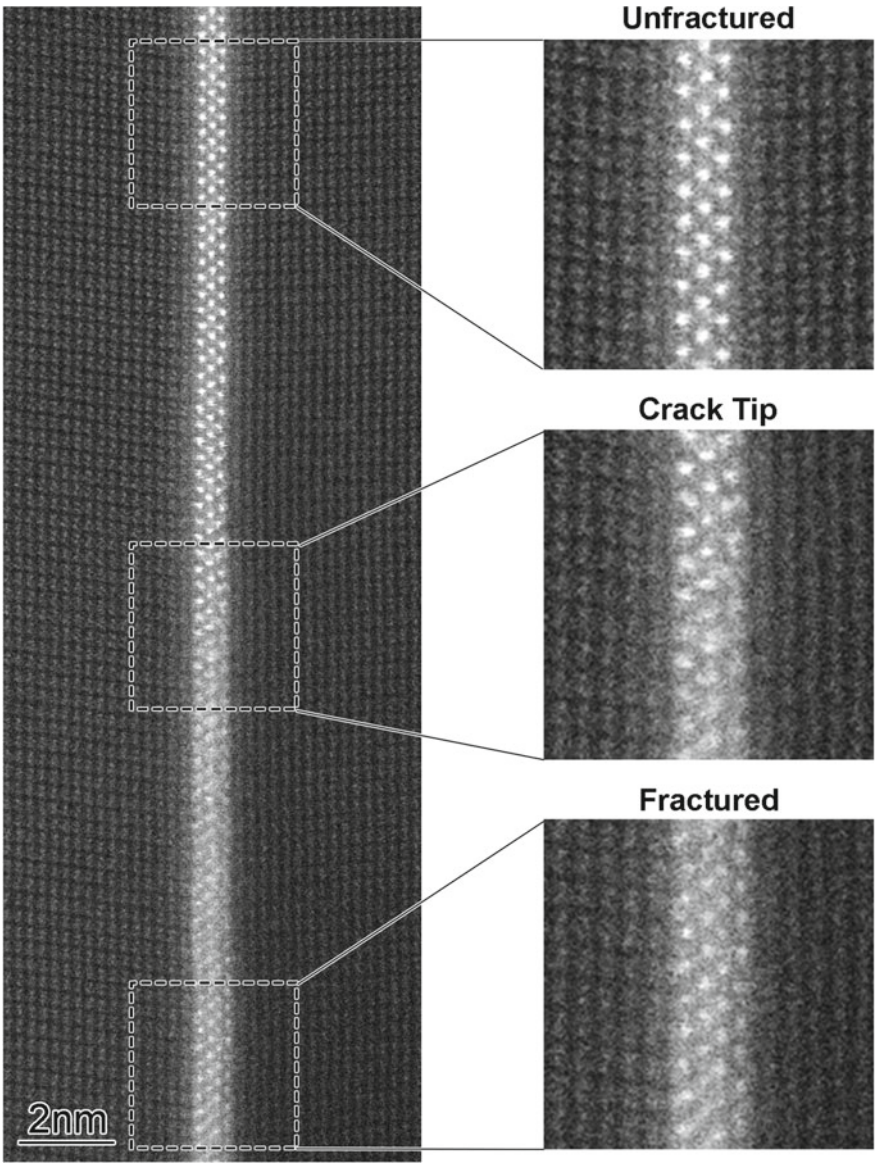

Fig. 7.16 HAADF-STEM image at the crack tip region. The bright contrasts correspond to Zr columns. In the unfractured region at the upper side, a Zr segragation phase in three layers is formed. The fractured region at the lower side appears to consist of four Zr layers, suggesting that the crack propagated within the Zr segregation phase and was divided into the left and right crystals. At the center of the image, contrasts of the Zr layer gradually change. The crack tip is expected to be located there (Kondo et al. 2019)

of four atomic layers, suggesting that the crack propagated within the Zr-segregated phase and the two crystals are slightly apart from each other with Zr layers on their surface. The contrast features of the Zr-segregated phase gradually change across the image center, and thus the crack tip is expected to be located around the image center.

Figure 7.17 shows a HAADF-STEM image of the fracture surface of the left crystal. The two layers of the Zr-segregated phase are observed. As seen in the intensity graph in the below panel, the top layer has a lower intensity than the second layer, although the two layers have a similar intensity in the unfractured area. Since the image intensity of an atomic column in HAADF-STEM depends on its atomic density, the number of atoms in the top layer should have decreased. That is likely to be half, because the left and the right crystals are symmetric. Therefore, it is considered that the crack propagated through the center layer of the Zr-segregated phase so as to equally distribute the center layer into the two symmetric crystals.

To investigate fracture mechanisms of the Zr-doped Σ13 grain boundary, three kinds of fracture paths for the grain boundary were examined by first-principles calculations. Figure 7.18a shows an optimized structure model of the Zr-doped Σ13 grain boundary viewing along the orthogonal directions of $[11\bar{2}0]$ and $[02\bar{2}1]$. Note that the structure model agreed well with the experimental image of the grain boundary. The dashed lines indicate three possible fracture paths, Zr-Al (straight), Zr-Zr (straight), and Zr-Zr (zigzag). The oxygen atoms are distributed so as not to produce a high-energy polar surface. The cleavage energies corresponding to these fracture paths were evaluated to be 4.66 Jm^{-2}, 3.61 Jm^{-2}, and 2.66 Jm^{-2}, respectively, indicating that the Zr-Zr (zigzag) path is energetically favorable. A comparison of an experimental image and optimized fracture surfaces formed by the Zr-Zr (zigzag) path and by Zr-Zr (straight) path is shown in Fig. 7.18b. The atomic positions of the Zr-Zr (zigzag) surface agree well with the experimental image, whereas those of the Zr-Zr (straight) surface do not. Therefore, the Zr-Zr (zigzag) path is energetically and structurally reasonable. It is considered that the cleavage energy is related to the atomic bonding of the grain boundary cut by a crack. The fracture due to Zr-Zr (straight) path produces 8 six-fold coordinated Zr on the two fracture surfaces, whereas Zr-Zr (zigzag) path produces 4 six-fold coordinated Zr and 8 seven-fold Zr (Kondo et al. 2019). A theoretical study suggested that zirconium oxides tend to have seven-fold or eight-fold Zr, and six-fold Zr requires relatively higher energy (Perdew et al. 1992). This would be the reason why the Zr-Zr (zigzag) path is selected for the grain boundary fracture.

7.4 Summary

In this report, we reviewed the atomic structure analysis of dislocations and grain boundary fracture surfaces of alumina by TEM/STEM. Using bicrystals with a low-angle grain boundary, $1/3 <11\bar{2}0>$ edge, $<1\bar{1}00>$ edge and $1/3 <\bar{1}101>$ mixed, and $1/3 <11\bar{2}0>$ screw dislocations were fabricated. The former three dislocations

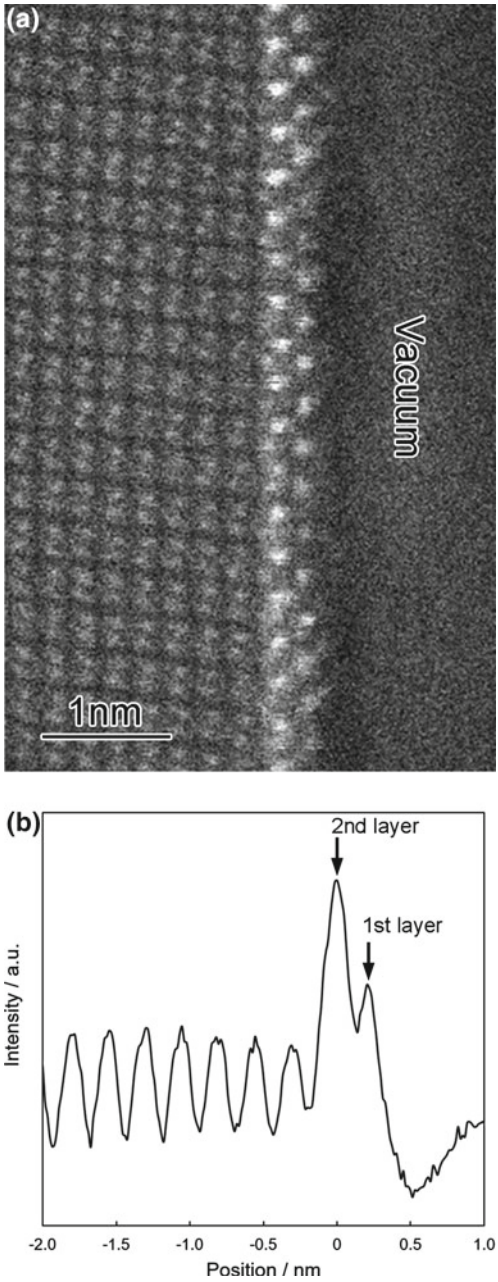

Fig. 7.17 **a** HAADF-STEM image of the fracture surface of the left crystal. Two Zr layers remain on the alumina crystal. **b** The intensity profile of the HAADF-STEM image in (**a**), where signals were integrated along the vertical direction. The intensity of the first layer is lower than the second layer, indicating that Zr atoms in the first layer were divided into two crystals (Kondo et al. 2019)

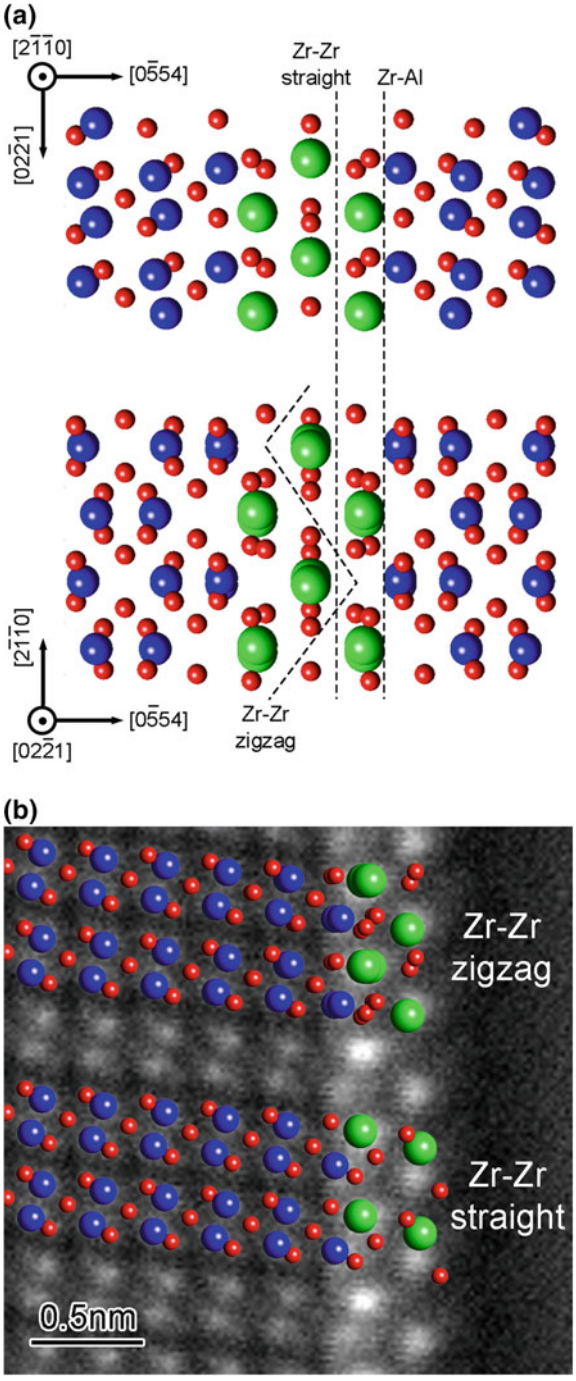

Fig. 7.18 **a** Atomic structure model of Zr-segregated $\{1\bar{1}04\}/<11\bar{2}0> \sum 13$ grain boundary of alumina. The upper and lower panels correspond to $[2\bar{1}\bar{1}0]$ and $[02\bar{2}1]$ projection, respectively. Fracture paths considered in the present study, Zr-Al, Zr-Zr (straight) and Zr-Zr (zigzag), are indicated by dashed lines. **b** Comparison of averaged experimental image and calculated fracture surfaces of Zr-Zr (straight) and Zr-Zr (zigzag). The Zr-Zr zigzag fracture surface agrees well with the experimental image (Kondo et al. 2019)

were found to be dissociated into partial dislocations with a stacking fault, whereas the last one has the perfect core. TEM/STEM analysis and theoretical calculations estimated the formation energy of $\{11\bar{2}0\}$, $\{1\bar{1}00\}$, and (0001) stacking faults to be approximately 0.3 Jm^{-2}, 0.4–0.5 Jm^{-2}, and 0.6–0.7 Jm^{-2}, respectively. Except for the $1/3 <11\bar{2}0>$ screw dislocation. In situ TEM nanoindentation technique was applied to induce basal slip in alumina. The 60° mixed $1/3 <11\bar{2}0>$ dislocation on the (0001) plane was introduced, and its core structure was characterized by STEM. It was found that the dislocation consists of two partial dislocations with $\{1\bar{1}00\}$ stacking fault. By this result, the core structures of representative segments (0°, 30°, 60°, and 90°) of the $1/3 <11\bar{2}0>$ basal dislocation were fully revealed. In addition, fracture of the Zr-doped $\{1\bar{1}04\}/<11\bar{2}0>$ $\sum 13$ grain boundary was induced by in situ TEM nanoindentation, and the fracture surfaces were characterized by STEM. It was found that the crack propagated along a zigzag path in order to equally divide the Zr-segregated phase into three atomic layers. Experimental image and theoretical calculations revealed that the fracture along the zigzag path forms stable Zr-O bonding on the fracture surfaces and gives the lowest cleavage energy in possible crack paths. It can be summarized that the TEM/STEM investigations of the dislocations and fracture surfaces extended our knowledge and understanding of deformation and fracture in alumina in terms of atomistic mechanisms.

Acknowledgements The authors gratefully thank Takahisa Yamamoto, Teruyasu Mizuguchi, Atsutomo Nakamura, Bin Feng, Jaike Wei, Yuki Kezuka, and Akihito Ishihara for collaborative works on dislocations and grain boundary fracture in alumina. A part of this study was supported by the Elements Strategy Initiative for Structural Materials (ESISM) (Grant No. JPMXP0112101000), KAKENHI (Grant Nos. JP17H06094, JP18K13981, and 19H05788) from the Japan Society for the Promotion of Science (JSPS), "Nanotechnology Platform" (Project No. JPMXP09A20UT0080) from the Ministry of Education, Culture, Sports, Science, and Technology in Japan (MEXT), and PRESTO "Nanomechanics" by Japan Science and Technology Agency (Grant No. JPMJPR1999).

References

Bilde-Sørensen JB, Thölen AR, Gooch DJ, Groves GW (1976) Structure of $<01\bar{1}0>$ dislocation in sapphire. Philos Mag 33:877–889. https://doi.org/10.1080/14786437608221921

Bilde-Sørensen JB, Lawlor BF, Geipel T, Pirouz P, Heuer AH, Lagerlöf KPD (1996) On basal slip and basal twinning in sapphire (α-Al_2O_3)–I Basal slip revisited. Acta Mater 44:2145–2152. https://doi.org/10.1016/1359-6454(95)00264-2

Christensen A, Carter EA (1998) First-principles study of the surfaces of zirconia. Phys Rev B 58:8050–8064. https://doi.org/10.1103/PhysRevB.58.8050

Chung DH, Simmons G (1968) Pressure and temperature dependences of isotropic elastic moduli of polycrystalline alumina. J Appl Phys 39:5316–5326. https://doi.org/10.1063/1.1655961

Firestone RF, Heuer AH (1976) Creep deformation of 0° sapphire. J Am Ceram Soc 59:13–19. https://doi.org/10.1111/j.1151-2916.1976.tb09379.x

Frank FC (1951) LXXXIII. Crystal dislocations.—Elementary concepts and definitions. Philos Mag 7th Ser 42:809–819. https://doi.org/10.1080/14786445108561310

Gieske JH, Barsch GR (1968) Pressure dependence of elastic constants of single crystalline aluminum oxide. Phys Stat Sol 29:121–131. https://doi.org/10.1002/pssb.19680290113

Heuer AH, Jia CL, Lagerlöf KPD (2010) The core structure of basal dislocations in deformed sapphire (α-Al_2O_3). Science 330:1227–1231. https://doi.org/10.1126/science.1192319

Ikuhara Y, Nishimura H, Nakamura A, Matsunaga K, Yamamoto T (2003) Dislocation structures of low-angle and near-Σ3 grain boundaries in alumina bicrystals. J Am Ceram Soc 86:595–602. https://doi.org/10.1111/j.1151-2916.2003.tb03346.x

Jhon MH, Glaeser AM, Chrzan DC (2005) Computational study of stacking faults in sapphire using total energy methods. Phys Rev B 71:214101. https://doi.org/10.1103/PhysRevB.71.214101

Kenway PR (1993) Calculated stacking-fault energies in α-Al_2O_3. Philos Mag B 68:171–183. https://doi.org/10.1080/01418639308226398

Kondo S, Ishihara A, Tochigi E, Shibata N, Ikuhara Y (2019) Direct observation of atomic-scale fracture path within ceramic grain boundary core. Nature Commun 10:2112. https://doi.org/10.1038/s41467-019-10183-3

Kresse G, Furthmüller J (1996) Efficiency of ab-initio total energy calculations for metals and semiconductors using a plane-wave basis set. Comp Mater Sci 1:15–50. https://doi.org/10.1016/0927-0256(96)00008-0

Kronberg ML (1957) Plastic deformation of single crystals of sapphire: Basal slip and twinning. Acta Metall 5:507–524. https://doi.org/10.1016/0001-6160(57)90090-1

Lagerlöf KPD, Mitchell TE, Heuer AH, Rivière JP, Cadoz J, Castaing J, Phillips DS (1984) Stacking fault energy in sapphire (α-Al_2O_3). Acta Metal 32:97–105. https://doi.org/10.1016/0001-6160(84)90206-2

Lagerlöf KPD, Heuer AH, Castaing J, Rivière JP, Mitchell TE (1994) Slip and twinning in sapphire. J Am Ceram Soc 77:385–397. https://doi.org/10.1111/j.1151-2916.1994.tb07006.x

Marinopoulos AG, Elsässer C (2001) Density-functional and shell-model calculations of the energies of basal-plane stacking faults in sapphire. Philos Mag Lett 81:329–338. https://doi.org/10.1080/09500830110039984

Miao B, Kondo S, Tochigi E, Wei J, Feng B, Shibata N, Ikuhara Y (2019) The core structure of 60° mixed basal dislocation in alumina (α-Al_2O_3) introduced by in situ TEM nanoindentation. Scripta Mater 163:157–162. https://doi.org/10.1016/j.scriptamat.2019.01.011

Mitchell TE, Pletka BJ, Phillips DS, Heuer AH (1976) Climb dissociation in sapphire (α-Al_2O_3). Philos Mag 34:441–451. https://doi.org/10.1080/14786437608222034

Nakamura A, Yamamoto T, Ikuhara Y (2002) Direct observation of basal dislocation in sapphire by HRTEM. Acta Mater 50:101–108. https://doi.org/10.1016/S1359-6454(01)00318-4

Nakamura A, Matsunaga K, Yamamoto T, Ikuhara Y (2006) Multiple dissociation of grain boundary dislocations in alumina ceramic. Philos Mag 86:4657–4666. https://doi.org/10.1080/14786430600812820

Nakamura A, Tochigi E, Shibata N, Yamamoto T, Ikuhara Y (2009) Structure and configuration of boundary dislocations on low angle tilt grain boundaries in alumina. Mater Trans 50:1008–1014. https://doi.org/10.2320/matertrans.MC200821

Perdew JP, Chevary JA, Vosko SH, Jackson KA, Pederson MR, Singh DJ, Fiolhais C (1992) Atoms, molecules, solids, and surfaces: applications of the generalized gradient approximation for exchange and correlation. Phys Rev B 46:6671–6687. https://doi.org/10.1103/physrevb.46.6671

Pletka BJ, Heuer AH, Mitchell TE (1974) Dislocation structures in sapphire deformed basal slip. J Am Ceram Soc 56:136–139. https://doi.org/10.1111/j.1151-2916.1974.tb11419.x

Shibata N, Chisholm MF, Nakamura A, Pennycook SJ, Yamamoto T, Ikuhara Y (2007) Nonstoichiometric dislocation cores in α-alumina. Science 316:82–85. https://doi.org/10.1126/science.1136155

Tochigi E, Shibata N, Nakamura A, Yamamoto T, Ikuhara Y (2008) Partial dislocation configurations in a low-angle boundary in α-Al_2O_3. Acta Mater 56:2015–2021. https://doi.org/10.1016/j.actamat.2007.12.041

Tochigi E, Shibata N, Nakamura A, Mizoguchi T, Yamamoto T, Ikuhara Y (2010) Structures of dissociated <1$\bar{1}$00> dislocations and {1$\bar{1}$00} stacking faults of alumina (α-Al2O3). Acta Mater 58:208–215. https://doi.org/10.1016/j.actamat.2009.08.067

Tochigi E, Shibata N, Nakamura A, Yamamoto T, Ikuhara Y (2011) Dislocation structures in a {$\bar{1}$104}/<11$\bar{2}$0> low-angle tilt grain boundary of alumina (α-Al2O3). J Mater Sci 46:4428–4433. https://doi.org/10.1007/s10853-011-5430-y

Tochigi E, Kezuka Y, Shibata N, Nakamura A, Ikuhara Y (2012) Structure of screw dislocations in a (0001)/[0001] low-angle twist grain boundary of alumina (α-Al2O3). Acta Mater 60:1293–1299. https://doi.org/10.1016/j.actamat.2011.11.027

Tochigi E, Nakamura A, Mizoguchi T, Shibata N, Ikuhara Y (2015) Dissociation of the 1/3<$\bar{1}$101> dislocation and formation of the anion stacking fault on the basal plane in α-Al2O3. Acta Mater 91:152–161. https://doi.org/10.1016/j.actamat.2015.02.033

Tochigi E, Findlay SD, Okunishi E, Mizoguchi T, Nakamura A, Shibata N, Ikuhara Y (2016) Atomic structure characterization of stacking faults on the { 1$\bar{1}$00} plane in α-alumina by scanning transmission electron microscopy. AIP Conf Proc 1763:050003. https://doi.org/10.1063/1.4961356

Tochigi E, Kezuka Y, Nakamura A, Nakamura A, Shibata N, Ikuhara Y (2017) Direct observation of impurity segregation at dislocation cores in an ionic crystal. Nano Lett 17:2908–2912. https://doi.org/10.1021/acs.nanolett.7b00115

Tochigi E, Mizoguchi T, Okunishi E, Nakamura A, Shibata N, Ikuhara Y (2018) Dissociation reaction of the 1/3<$\bar{1}$101> edge dislocation in α-Al2O3. J Mater Sci 53:8049–8058. https://doi.org/10.1007/s10853-018-2133-7

Sasaki T, Shibata N, Matsunaga K, Yamamoto T, Ikuhara Y (2012) Direct observation of the cleavage plane of sapphire by in-situ indentation TEM. J Ceram Soc Jpn 120:473–477. https://doi.org/10.2109/jcersj2.120.473